Investigation of the interphase structure in polyamide 6–matrix, multi-scale composites

Petrény R., Almásy L., Mészáros L.

Composites Science and Technology 225 (2022) 109489

Contents lists available at ScienceDirect

Composites Science and Technology

journal homepage: www.elsevier.com/locate/compscitech

Investigation of the interphase structure in polyamide 6–matrix, multi-scale composites

Roland Petrény [a], László Almásy [b], László Mészáros [a,c,*]

[a] Department of Polymer Engineering, Faculty of Mechanical Engineering, Budapest University of Technology and Economics, Műegyetem rkp. 3, Budapest, H-1111, Hungary
[b] Institute for Energy Security and Environmental Safety, Centre for Energy Research, Konkoly Thege Miklós út 29-33, Budapest, H-1121, Hungary
[c] MTA–BME Research Group for Composite Science and Technology, Műegyetem rkp. 3, Budapest, H-1111, Hungary

ARTICLE INFO

Keywords:
Hybrid composites
Carbon fibres
Carbon nanotubes
Interphase
Injection moulding

ABSTRACT

In this study, we investigated the dispersion of carbon nanotubes and the interphases formed around them in nanocomposites with a polyamide 6 matrix (with carbon nanotube reinforcement) and hybrid composites with the same matrix, reinforced with carbon nanotubes and carbon fibers. Small-angle neutron scattering (SANS) experiments showed that carbon fibers effectively increased the dispersion of the carbon nanotubes. The average size of the carbon nanotube aggregates were significantly smaller, but the reinforcement–matrix interface area was larger in the hybrid composites than in the nanocomposites. Nanotube dispersion had a significant effect on the crystalline structure; the X-ray diffraction patterns showed that in the hybrid composites, the crystallites grew epitaxially on the surface of the well-dispersed carbon nanotubes, which resulted in decreased average crystallite size. In the hybrid composites, the smaller crystallites inferred a larger rigid amorphous fraction in the matrix. The larger interphase fraction in the hybrid composites also led to better mechanical performance.

1. Introduction

The investigation of the microstructure of nanocomposites with a polymer matrix has became a major research area in the past two decades. Among nanoparticles, carbon nanotubes (CNTs) are used most widely, due to their high modulus, tensile strength, flexibility, and good thermal and electric conductivity. However, for the greatest property-modifying effect of CNTs in composites, they have to be uniformly dispersed in the polymer matrix, so that the interface between the nanoparticles and the matrix is the largest. Thus, stronger adhesion develops between them even if compatibility is low [1–6].

An increasingly popular method for dispersing the nanotubes in a polymer matrix is to associate them with micro-sized reinforcement, where the micro-sized reinforcement improves the dispersion of the nanoparticles during melt processing. As the fibers increase melt viscosity, higher shear in the melt efficiently helps the dispersion of the nanoparticles. In such a composite, the microfibers have a strong reinforcing effect, which is further increased by the nanotubes. One of the greatest advantages of this method is that it can be used with thermoplastic matrix materials, therefore these hybrid composites can be manufactured with the most productive melt-processing methods, such as extrusion and injection molding [7–10].

In our previous paper [11], we showed by scanning electron microscopy (SEM) that hybrid composites containing carbon fiber and CNT in a polyamide 6 (PA6) matrix have fewer aggregates on the fracture surfaces compared to composites containing only CNT. The problem with these results is that the SEM images provide information only about the fracture surface, which does not necessarily represent the volumetric structure of the composites.

In order to understand the property-modifying mechanisms of CNT in polymer composites, we should characterize the dispersion of nanotubes and the structure of the nanotube aggregates. So far, relatively few papers have investigated the nanoparticle structure in the polymer matrix using small angle neutron scattering (SANS). SANS can resolve the structure of the interfaces between the matrix and the reinforcing material in nano- and hybrid composites. Dimensional and shape information can be obtained about inhomogeneities in the 1–100 nm range with the use of SANS. As opposed to conventionally used microscopic methods, SANS provides information averaged over the total volume of the sample. An important morphological feature of these

* Corresponding author. Department of Polymer Engineering, Faculty of Mechanical Engineering, Budapest University of Technology and Economics, Műegyetem rkp. 3, Budapest, H-1111, Hungary.
E-mail address: meszaros@pt.bme.hu (L. Mészáros).

https://doi.org/10.1016/j.compscitech.2022.109489
Received 18 November 2021; Received in revised form 24 March 2022; Accepted 26 April 2022
Available online 30 April 2022

composite materials is the character of the interface zone between the reinforcement and the matrix; it can be either an irregular, fractal-like or a diffuse, continuously varying interphase [12–15].

Not only the reinforcements and their dispersion influence the mechanical properties of nano- and hybrid composites. Due to the interactions (secondary bonds, entanglements) between the matrix and the reinforcement, an interphase is formed around the reinforcing materials, which also modifies the properties of the composite. In previous studies, the role of these interphases on the mechanical properties of composites was investigated, and the micromechanical models created demonstrated that the mechanical properties of composites can be more accurately designed by taking into account the interphases and the dispersion of nanoparticles [16–18].

However, these models do not address the morphological structure of the interphases which determines their mechanical properties in the given matrix–reinforcement system. Several papers have shown that in nano- and hybrid composites, the reinforcing additives may have a crystalline nucleating effect in semi-crystalline matrices. In some studies, X-ray diffraction analysis (XRD) indicated that the surface structure of the nanoparticles may influence the direction of crystal growth, i.e. the crystallites grew epitaxially on the nanoparticles (for example in composites containing CNT and graphene). As a result, a semi-crystalline interphase forms, which partially surrounds the reinforcement. As a significant proportion of the crystallites grow on the surface of the reinforcing particles, the size distribution of the particles and the remaining aggregates have a significant influence on the structure of the interphase [19–23].

In composites with a semi-crystalline matrix, three different phases can be distinguished in the matrix: the crystalline, the mobile amorphous and the rigid amorphous phase. The rigid amorphous phase can form around either the reinforcement or the crystallites. Therefore, the interphase around the nanoparticles can be a single-layer rigid amorphous or a double-layer interphase, where the inner structure is semi-crystalline and the outer structure is rigid amorphous. With the use of modulated differential scanning calorimetry (MDSC), the ratio of the crystalline, mobile amorphous and rigid amorphous phases can be determined. With this technique, complemented with SANS and XRD, a deep structural analysis on composite materials can be performed, which can provide a better understanding of the structure–property relationships in hybrid composites [20,24–27].

The aim of the present research is to investigate the effect of nanoparticle dispersion on the morphological structure of the matrix material in carbon nanotube–reinforced polyamide 6–matrix nanocomposites, and of carbon nanotube and carbon fiber–reinforced hybrid composites, with special emphasis on the interphases in the reinforcement environment. A further aim was to investigate the influence of this microstructure on tensile mechanical properties. With these results, it is possible to gain a deeper understanding of the relationship between structure and strength properties, which may help to refine micromechanical models.

2. Materials and methods

To investigate the effect of the nano- and the hybrid reinforcement on the structure of the composites, we manufactured two series of samples: polyamide 6 with 0.00, 0.25, 0.50, 0.75, and 1.00 wt% carbon nanotube content (PA, PA+0.25CNT, PA+0.5CNT, PA+0.75CNT, PA+1CNT), and with 30 wt% carbon fiber and 0.00, 0.25, 0.50, 0.75, and 1.00 wt% nanotube content (PA, PA+30CF+0.25CNT, PA+30CF+0.5CNT, PA+30CF+0.75CNT, PA+30CF+1CNT). The SCHULAMID 6 MV 13 F polyamide 6 matrix was produced by A. Schulman GmbH (Kerpen, Germany). It has a density of 1.13 g/cm^3 and a melt flow index (MFI) of 14.7 g/10 min (230 °C, 2.16 kg). The nanoparticles were Nanocyl NC7000 multi-walled carbon nanotubes (Fig. 1 a), produced by Nanocyl SA, with an average diameter of 9.5 nm, an average length of 1.5 μm, and a specific surface area of 250–300 m^2/g. The carbon purity of the nanotubes was 90%, and the transition metal oxide content was less than 1%. The microfibrous reinforcement was Panex 35 Chopped Pellet 95 carbon fiber (Fig. 1 b) produced by Zoltek Zrt. (Nyergesújfalu, Hungary), which has a diameter of 8.3 μm, a length of 6 mm, and a density of 1.81 g/cm^3 with silane surface treatment, designed for polar polymers.

The scanning electron microscope (SEM) images of the reinforcing materials were taken with a JEOL 6380 LA scanning electron microscope after sputtering of the surfaces with a thin layer of gold.

The matrix was dried at 80 °C for 4 h before processing. The reinforcing materials were then mechanically mixed with it. The compounds were prepared with a Labtech LTE 26–44 twin-screw extruder at 230–240 °C at 25 rpm. The granules were dried again at 80 °C for 4 h, and the EN ISO 527–2:2012 dumbbell type specimens were injection molded with an Arburg Allrounder 370 S 700–290 injection molding machine. Melt temperature was 255–275 °C, mold temperature was 80 °C and injection pressure was 1200 bar. After compounding and injection molding, the carbon fibers were fragmented to a mean length of 115 μm and oriented at an angle of 25° to the load direction in the carbon fiber–reinforced composites based on one of our studies [28]. This orientation was homogeneous in the full cross-section of the samples and did not change when carbon nanotubes were added.

For the SANS and XRD analysis, the 20 mm × 20 mm, 2 mm thick samples were machined with a Roland MDX-540 4-axis milling machine from the gripping end of the injection molded tensile specimens.

The SANS experiments were performed on the Yellow Submarine instrument at the Budapest Neutron Centre [29,30]. Mean neutron wavelength was 1.04 nm, and the detector–sample distance was 535 cm. The experiments were performed at room temperature, with a counting time of 1 h.

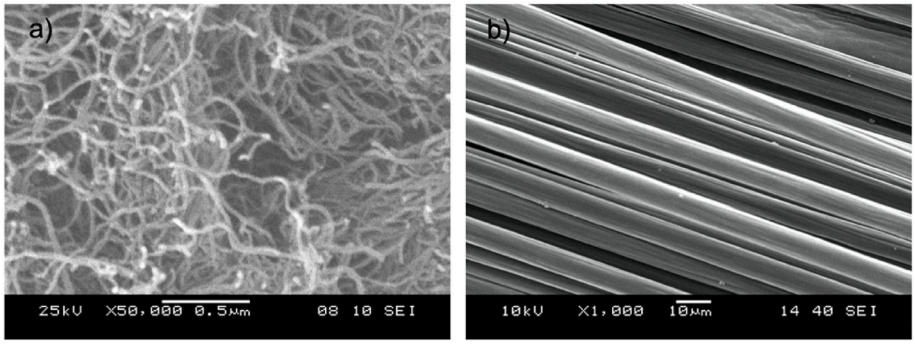

Fig. 1. Scanning electron microscope images a) of the carbon nanotubes and b) of the carbon fibers.

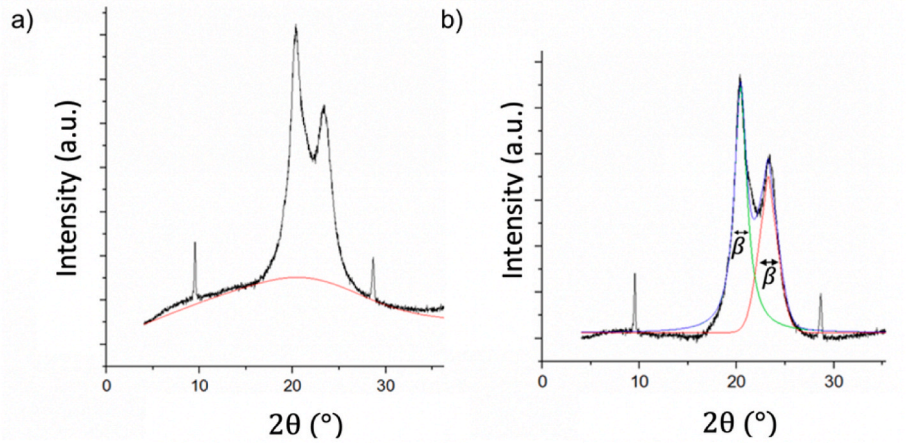

Fig. 2. Determining the amorphous baseline and decomposition of the peaks.

X-ray diffraction analysis was performed on a PANalytical X'pert Pro MPD X-ray diffractometer equipped with a Cu K_α radiation source and an X'Celerator detector. The amorphous baseline of the X-ray diffractograms was determined with the asymmetric least squares method (Fig. 2 a.). To investigate the ratio of the number of α_1 and α_2 crystal planes and the average crystallite size perpendicular to the related planes, we separated the diffraction peaks with the pseudo-Voigt model (Fig. 2 b.). The diffraction peaks at 9.4° and 29° belong to talc, which was also present in the pure matrix material, and was not considered for further investigation [31–33].

The average size perpendicular to the crystal planes α_1 and α_2 was calculated from the half-width of the separated peaks with the Scherrer equation (1):

$$L = \frac{K\lambda}{\beta \cos\theta} \tag{1}$$

where L is the average size perpendicular to the given crystal plane, $K = 0.89$ is a constant, β is the half-width of the given diffraction peak, and θ is the diffraction angle [34].

The calorimetric tests were performed on a TA Instruments Q2000 differential scanning calorimeter (DSC) in a N_2 atmosphere (the flow speed was 50 ml/min), in modulated DSC (MDSC) mode. The test temperature range was 0–250 °C, the heating and cooling rate was 5 °C/min, the amplitude of modulation was 1 °C and its period was 60 s. The mass of the samples was 10–15 mg. 3 samples of each material were measured and the results averaged. Lamellar thickness was calculated with the Gibbs-Thomson equation (2):

$$l = \frac{2\sigma_e}{\Delta H_m \rho_c \left(1 - \frac{T_m}{T_{m,\infty}}\right)} \tag{2}$$

where l is lamellar thickness, $\sigma_e = 5.7 \bullet 10^4 \frac{J}{m^2}$ is the surface free energy of the crystallite, $\Delta H_m = 241 \frac{J}{g}$ is the enthalpy of crystal melting, $\rho_c = 1.230 \frac{g}{m^3}$ is the density of the crystallite, $T_{m,\infty} = 533\ K$ is the theoretical melting point of an infinitely large crystallite and T_m is the melting peak from the measured DSC curve [35–37].

The volume ratio of the rigid amorphous phase (φ_{RAF}) in the matrix is (3) [24]:

$$\varphi_{RAF} = 1 - \varphi_{MAF} - \varphi_C \tag{3}$$

where φ_{MAF} is the volume ratio of the mobile amorphous fraction, φ_C is the crystalline fraction. For this, the crystallinity can be calculated with the following equation (4):

$$\varphi_C = \frac{\Delta H}{\Delta H_0 (1 - \varphi_R)} \tag{4}$$

The related ΔH is the crystalline melting enthalpy as determined by DSC, ΔH_0 is the melting enthalpy of theoretically 100% crystalline polyamide 6, and $\varphi_R$is the weight ratio of the reinforcing material [24].

The volume ratio of the mobile amorphous fraction is calculated as follows (5):

$$\varphi_{MAF} = \frac{\Delta C_p}{\Delta C_{p,\,0}} \tag{5}$$

where $\Delta C_p$is the specific heat increment of the semi-crystalline polymer and $\Delta C_{p,\,0}$ is the specific heat increment of the fully amorphous polymer in the glass transition temperature range. In the case of polyamide 6, according to the literature, $\Delta C_{p,\,0} = 0.475 \frac{J}{g°C}$ [24].

Tensile tests were carried out on 5 specimens/material on a Zwick Z005 universal tensile tester, according to EN ISO 527. The tensile moduli were determined with the linear regression line fitted between 0.05% and 0.25% strain. Crosshead speed was 5 mm/min and gauge length was 110 mm. Before testing, the specimens were conditioned at 50% rh and 25 °C for 8 weeks.

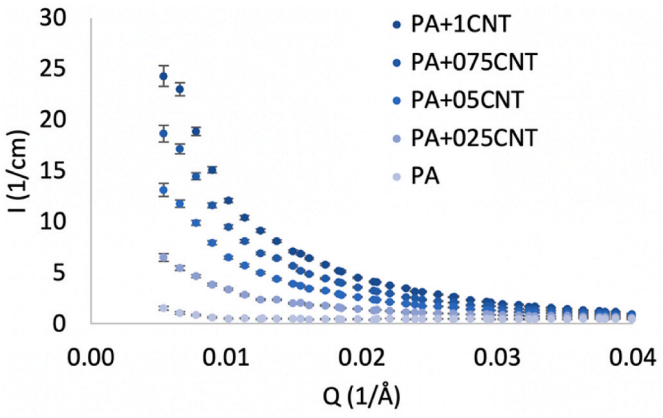

Fig. 3. Scattering plot of the pure PA6 and the nanocomposites.

3. Results and discussion

3.1. Small-angle neutron scattering

In composites, the small angle neutron scattering signal comes from the interfaces between phases with different scattering length densities, such as the organic polymer and the carbon nanotube or carbon fiber. When the carbon additives are not fully dispersed, bulk carbon regions remain. The polymer phase does not penetrate into these regions, therefore the carbon–polymer interface is smaller than the surface of the carbon particles [12,38]. Fig. 3 shows the scattering curves of the nanocomposites. It is visible that scattering intensity increased with increasing nanotube content in the nanocomposites, i.e., higher nanotube content results in a larger nanotube–matrix interface.

In the scattering curves of the hybrid composites (Fig. 4), the scattering intensity increased when carbon fiber was added to the polyamide. The addition of nanotubes resulted in a further increment, which was larger than in the case of nanocomposites. The results indicate that the sum of the scattering interfaces in the hybrid composites is larger than the sum of the interfaces of the composites containing only carbon fibers or nanotubes, i.e., the carbon fibers helped to disperse the nanotubes more uniformly in the matrix.

Carbon fibers and carbon nanotubes consist of the same atoms. They have similar structures, so their scattering length densities should be nearly the same. Polyamide molecules contain many hydrogen atoms, which means that their scattering length densities are much lower, so the contrasts at the carbon fiber–matrix interface and the carbon nanotube–matrix interface are of the same order of magnitude and almost identical. Thus, with the use of neutron scattering, the interfaces belonging to the different carbon-based reinforcements can only be distinguished indirectly [13].

In order to separate the contribution of the CNT–polymer interface to the scattering pattern, we subtracted the intensity data of pure polyamide from the scattering data of nanocomposites. In the case of hybrid composites, the scattering data of the polyamide containing only carbon fibers was subtracted from the scattering data of the hybrid composites, assuming that the carbon fibers were well-dispersed and their dispersion was not affected by the presence of nanoparticles [5,24]. The scattering data so modified are shown in Fig. 5. The scattering intensity increment for hybrid composites is higher compared to the nanocomposites. Moreover, a synergistic effect was observed for hybrid composites—with increasing nanotube content, the increments are larger. It is striking that a nanotube content of 0.75 wt% in the nanocomposites resulted in the same scattering intensity as 0.25 wt% nanotube content in the hybrid composites. In composites containing 1.00 wt% nanotubes, the scattering intensity almost doubled if carbon fiber was also present in the composite, indicating the significant increase in the nanotube–polymer interface.

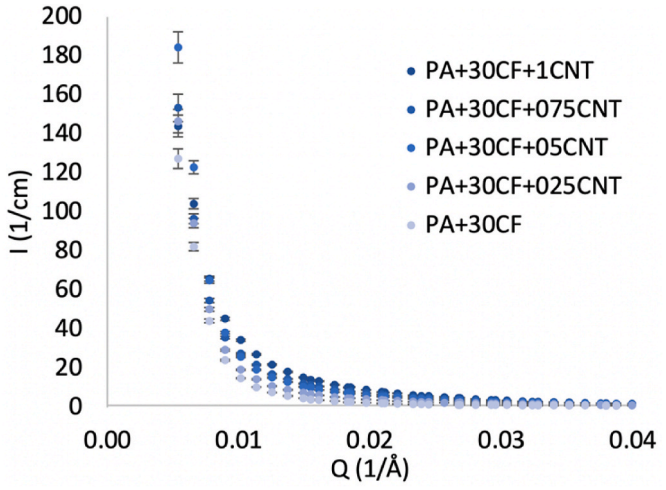

Fig. 4. Scattering plot of the carbon fiber–reinforced and the hybrid composites.

These results indicate that the sum of the nanotube–polymer interfaces in the hybrid composites is larger than in the nanocomposites (without the carbon fibers), which proves that the carbon fibers helped to disperse the nanotubes more uniformly in the matrix.

The small-angle part of the curves also contains information about the average size of the scattering nanotubes or their aggregates in the sample, which is most commonly described with the Guinier equation [39]:

$$I(Q) = I(0) \bullet e^{-\frac{(Q \bullet R_g)^2}{3}}$$

where I(Q) is the scattering intensity as a function of the scattering vector, Q is the scattering vector, I (0) is the intensity at zero scattering angle extrapolated from the linear fit, and R_g is the radius of gyration. To calculate the radius of gyration, we plotted the measured data as ln (I (Q)) as a function of Q^2 (Fig. 6). A straight line can be fitted on the data scaled this way, the slope of which gives R_g^2. This line was fitted with the use of the least squares method to the first 10 measured points (in the Q interval between 2.8×10^{-5} and 1.57×10^{-4} $Å^{-2}$), with $R^2 > 0.95$.

For spherical particles, the radius of gyration can be transformed to the average radius of the scattering objects [39]:

$$R = R_g \sqrt{\frac{5}{3}}$$

Fig. 7 shows the average radius of the scattering objects (nanotubes or their aggregates) calculated with the Guinier approximation. In the nanocomposites, the average size of the objects was larger than in the hybrid composites, and increased with carbon nanotube content, indicating that the nanotubes formed larger aggregates. The average size of scattering objects was smaller in the hybrid composites. This shows that the carbon fibers helped break up nanotube aggregates and provided more uniform nanotube dispersion.

3.2. X-ray diffraction

As the micro- and nanosized reinforcing particles often act as crystal nucleating agents, their dispersion in the matrix significantly affects the crystalline structure, especially in the case of nanoparticles, due to their high surface/volume ratio. If there are carbon nanotubes in the matrix, the matrix–nanotube interface may act as the starting point of crystal nucleation, resulting in a semi-crystalline interphase that partially surrounds them.

We analyzed the crystalline structure of nano- and hybrid composites by X-ray diffraction. The peaks at 20.2° and 23.4° in the diffractograms (Fig. 8 a, b) show that all of the samples contain only α-crystal modifications and the γ-crystal modification cannot be detected in the matrix. The diffraction peak at 20.2° is related to the α_1 crystal planes (200), while the peak at 23.4° is related to the α_2 crystal planes (202) + (020) [21].

In the pure matrix material, the (202) + (020) crystal planes are most common, while in the nanocomposites, the (200) crystal planes are dominant, suggesting that the PA chains are folded to the surface of the carbon nanotubes. This is because the distance between the crystal planes (200) is 0.44 nm, which is nearly twice the spacing between carbon atoms on the surface of carbon nanotubes (0.426 nm, Fig. 8 c) therefore epitaxial crystal growth can start from the surface of the carbon nanotubes [22]. Brosse et al. [20] also showed that the reflection plane (200) formed in PA6 is perpendicular to the surface of carbon nanotubes, suggesting that a semi-crystalline interphase is formed around the carbon nanotubes. The chirality of the carbon nanotubes significantly affects the epitaxial crystallization. The Nanocyl NC7000 carbon nanotubes were unsorted, so chirality was not uniform. The

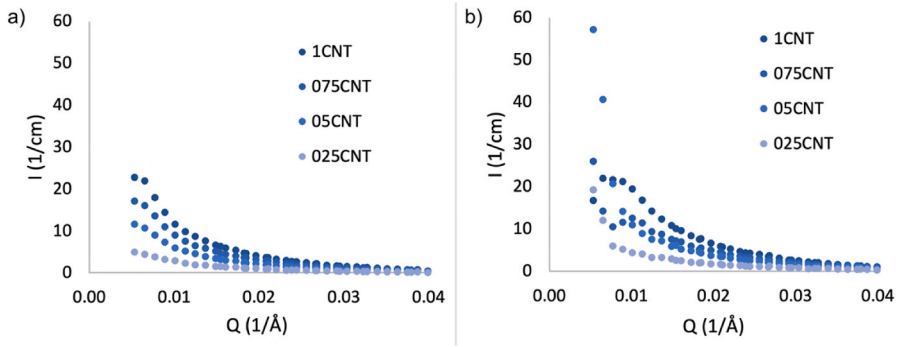

Fig. 5. Scattering plot of the carbon nanotubes that are a) in the nanocomposites and b) in the hybrid composites.

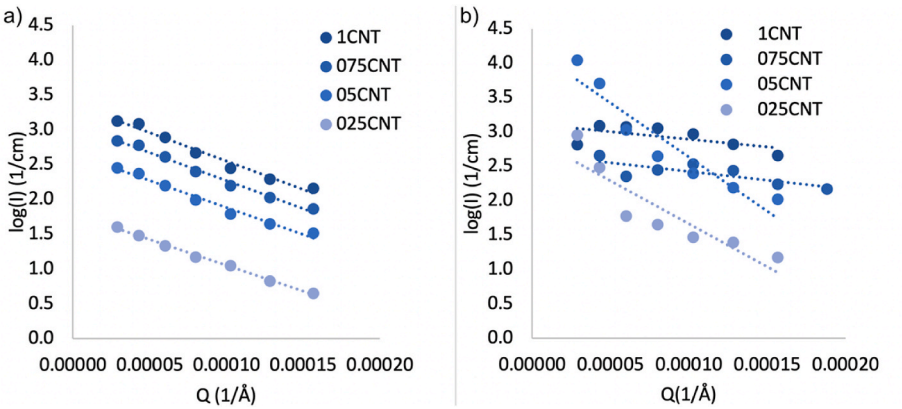

Fig. 6. Guinier analysis of the scattering data of a) the nanocomposites and b) the hybrid composites.

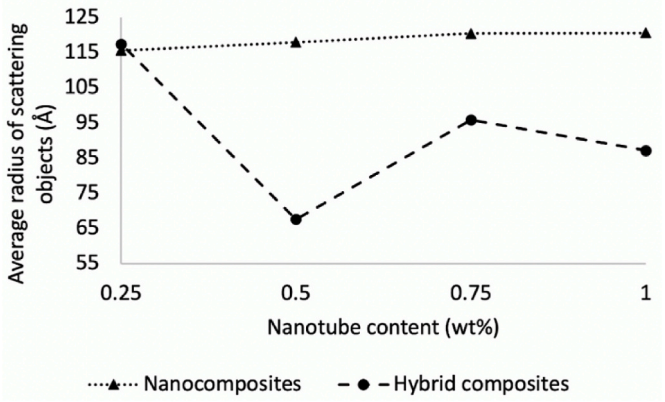

Fig. 7. The average radius of the scattering nanotubes or their aggregates in the nano- and hybrid composites.

nanotubes are present in the composite in large quantities (approximately 1.6×10^{10} nanotubes/mm^3 for 0.25 wt% CNT content). Therefore, carbon nanotubes with the right chirality (CNT (10,10)) should occur in certain numbers. Since their effect is significant, even if there are not many of them, they have a decisive influence on epitaxial crystallization.

The diffractograms of the carbon fiber–reinforced composites show that carbon fibers significantly increase the proportion of α_2 crystal planes characteristic of pure PA6. An increasing number of α_2 planes are usual for the transcrystalline layer surrounding the fibers. It can be assumed that, similarly to nanotubes, carbon fibers form a semi-crystalline interphase around themselves. In order to get a more accurate picture of the crystalline interphase on the surface of nanotubes, we determined average lamellar thickness with DSC tests (Table 1).

The average lamellar thickness of the nano- and hybrid composites was approximately 5 nm, and did not change significantly as the ratio of the components was varied. Based on the XRD results, lamellar thickness should be interpreted as the crystallite size parallel with nanotube length (Fig. 8 c).

The proportion of α_1 crystal planes in nanocomposites was higher in all cases than in pure PA6; however, it did not increase with increasing nanotube content (Fig. 9). This is because the outer surface of the nanotube aggregates, on which the polymer chains were able to fold, had a stochastic size distribution.

In hybrid composites, the α_2 crystal planes were dominant due to the large amount of carbon fiber, and the proportion of α_1 crystal planes also decreased with increasing nanotube content. This may be because the α_2 crystal planes forming around the carbon fibers and the associated rigid amorphous interphase occupied such a large volume in the matrix that there were not enough mobile molecular segments around the nanotubes to start crystallization on the surface of the nanotubes.

In the presence of nanotubes, the size perpendicular to the α_1 crystal planes increased significantly in both nano- and hybrid composites, while the increase in nanotube content affected the shape of the resulting crystallites differently in nano- and hybrid composites (Fig. 10). The size in the α_1 direction is proportional to the number of molecular folds, while the size in the α_2 direction is proportional to the number of aligned lamellae, i.e., the thickness of the crystalline interphase (the lamellar thickness is nearly constant based on the DSC tests). In the nanocomposites, the size perpendicular to the α_1 crystal planes increased. In contrast, the size perpendicular to the α_2 crystal planes decreased as a result of the nanotube content. If there are aggregates in the system, a small part of the surface of nanotubes is in contact with the

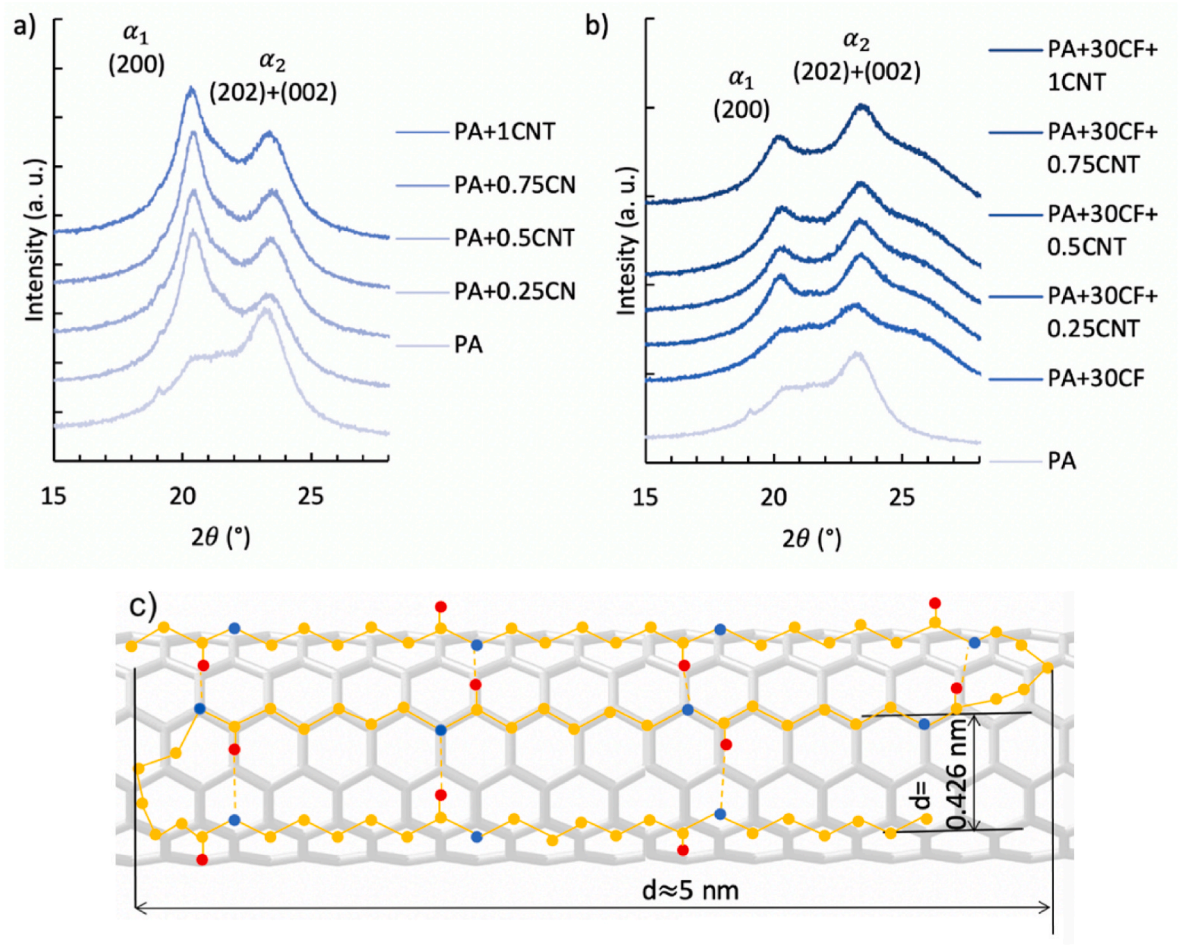

Fig. 8. X-ray diffraction patterns of a) the PA6 and the nanocomposites, b) the fiber-reinforced and hybrid composites, c) the model of epitaxial crystal growth on the surface of well-dispersed carbon nanotubes [40].

Table 1
Lamellar thickness of the nano- and hybrid composites calculated from the first and second heat-up.

Name	Lamellar thickness, first heat-up (nm)	Lamellar thickness, second heat-up (nm)
PA	4.99	4.97
PA+0.25CNT	5.28	5.04
PA+0.5CNT	5.08	4.96
PA+0.75CNT	5.02	4.94
PA+1CNT	5.10	5.00
PA+30CF	5.08	4.93
PA+30CF+0.25CNT	5.14	5.10
PA+30CF+0.5CNT	5.08	4.96
PA+30CF+0.75CNT	5.04	5.02
PA+30CF+1CNT	5.11	5.04

matrix only, so that the number of α_1 oriented crystal planes can grow only on a relatively small nanotube surface. The size perpendicular to the α_2 planes is reduced compared to the pure matrix material due to the effect of nanotubes, which may be because the number of lamellae in the spherulites of the pure matrix material is larger than in the crystalline interphase surrounding the nanotube aggregates.

The size of the α_1 planes is larger in hybrid composites than in nanocomposites and increases with increasing nanotube content, while the size of the α_2 planes is smaller and does not change significantly with increasing nanotube content. In a well-dispersed system, the crystalites can surround the individual nanotubes completely in the radial (α_1) direction. However, due to the uniform distribution of nanotubes in the volume and the high rigid amorphous phase ratio, there is not enough free volume to allow this crystalline interphase to thicken in the α_2 direction.

3.3. DSC tests

In the composites with a PA6 matrix, mobile and rigid amorphous fractions can be distinguished besides the crystalline fraction. The rigid amorphous fraction can connect either to the reinforcing material or to the crystallites. As its mechanical properties differ from the mechanical properties of the mobile amorphous fraction, its volume fraction can influence the macroscopic mechanical properties of the composite. The crystalline structure in the matrix influences the volume ratio of the rigid amorphous phase, and thereby it has an even larger impact on the mechanical properties of the composite.

In the nanocomposites, despite the moderate increase in crystallinity, the ratio of the rigid amorphous fraction decreased (Fig. 11). This can be explained by the larger crystallite size discussed early (Fig. 10), i.e., the larger crystallites have a smaller surface–volume ratio, thereby the rigid amorphous fraction connected to the surface of the crystallites should also be smaller.

In the hybrid composites, both crystallinity and the rigid amorphous fraction increased (Fig. 12) due to the more uniform dispersion of the nanotubes, resulting in a smaller crystallite size (Fig. 10). The crystallites grown on the surface of the uniformly dispersed carbon nanotubes are smaller and have a large surface–volume ratio, thus the rigid amorphous fraction connected to them takes a larger volume in the matrix.

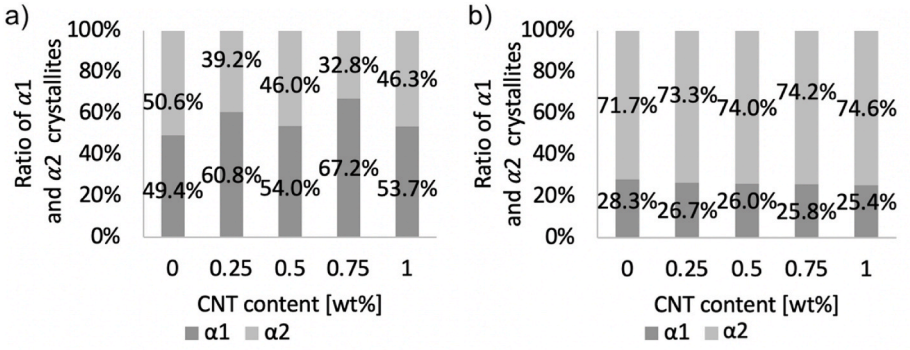

Fig. 9. Ratio of the α_1 and α_2 crystallites a) in the PA6 and in the nanocomposites, b) in the fiber-reinforced and hybrid composites.

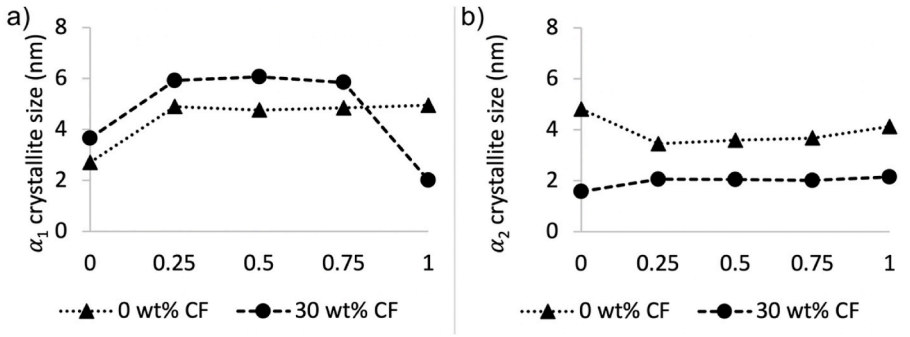

Fig. 10. Average size of a) the $\alpha_1$crystallites and b) α_2 crystallites in the PA6, the nanocomposites, the fiber-reinforced, and hybrid composites.

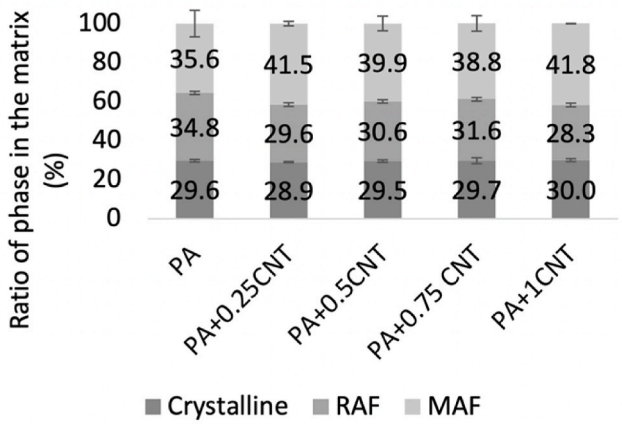

Fig. 11. Proportion of the crystalline, the rigid amorphous and the mobile amorphous fractions in the PA6 and the nanocomposites.

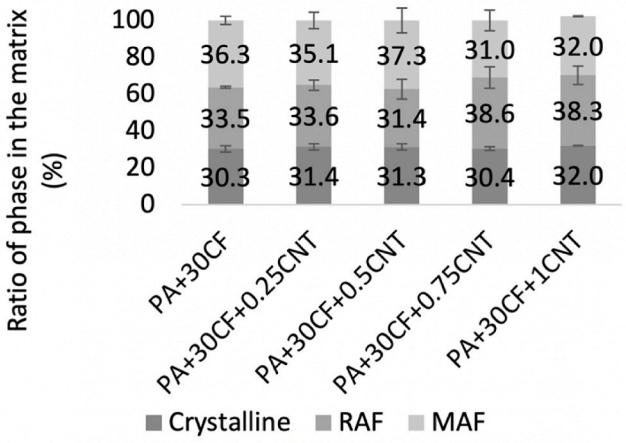

Fig. 12. Proportion of the crystalline, rigid amorphous and mobile amorphous fractions in the fiber-reinforced PA6 and the hybrid nanocomposites.

Based on this morphology, a double-layer interphase model can be constructed (Fig. 13). The inner layer is the crystallites grown on the reinforcement surface, and the outer layer is the rigid amorphous fraction connected to it. In the hybrid composites, both the crystalline and the rigid amorphous volume fraction increased, which indicates that the interphase fraction also increased; this explains the better matrix–reinforcement connection compared to the nanocomposites.

3.4. Tensile mechanical properties

The tensile mechanical properties of the nano- and hybrid composites were in good agreement with the morphological characteristics of the materials. When the materials did not contain carbon fibers, the tensile strength and tensile modulus decreased significantly with higher nanotube content, as the carbon nanotube aggregates functioned as the starting point of failure (Fig. 14). This is because melt processing technologies cannot provide a satisfactory dispersion of the CNTs in composites. When carbon fibers were also present in the composites, tensile strength remained on the same level, while modulus increased with increasing nanotube content. In the case of hybrid composites, modulus increased by around 600 MPa. It means that simply adding micro-sized carbon fibers to the composite improves the dispersion of the nanotubes, which is also reflected in the mechanical properties. Well-dispersed carbon nanotubes can develop a better connection with the matrix; moreover, the larger fraction of crystalline and rigid amorphous interphase may have an additional stiffening effect.

In one of our previous articles [11], we investigated the moisture-dependent tensile and creep properties of these materials, and

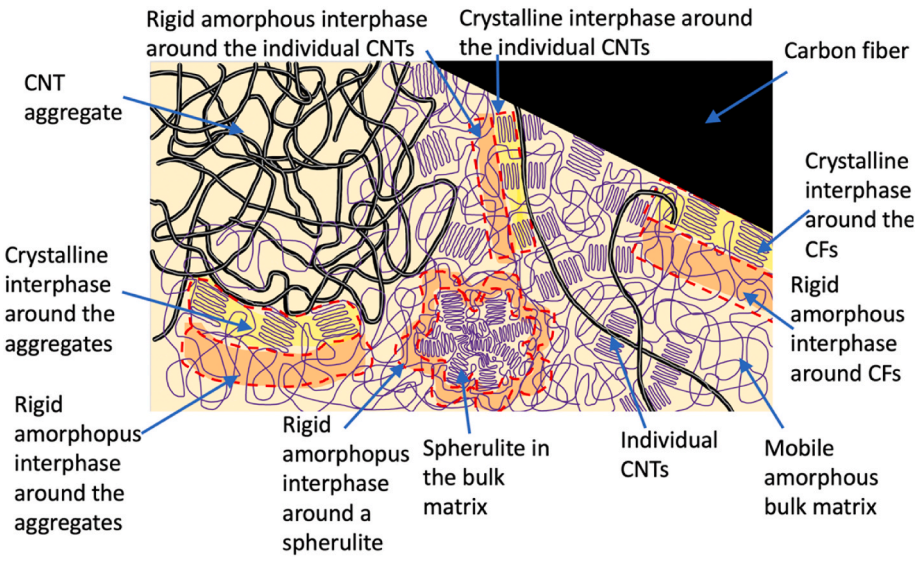

Fig. 13. The structural units and interphase model of the nano- and hybrid composites.

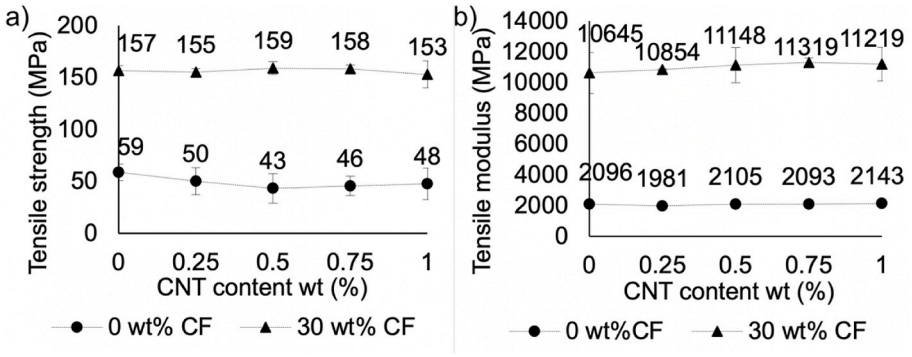

Fig. 14. a) tensile strength and b) tensile modulus of the nano- and hybrid composites.

found that, especially at higher relative humidities, nanotubes had a positive effect on the tensile properties when they were combined with micro-sized reinforcement. Creep properties improved even more.

4. Summary

In this paper, we investigated the interphase structure and its dependence on carbon nanotube dispersion in carbon nanotube and carbon fiber–reinforced nano- and hybrid composites. The small-angle neutron scattering experiments showed that the carbon fibers effectively helped the dispersion of the carbon nanotubes. In the hybrid composites, the average size of the carbon nanotube aggregates was significantly smaller. At the same time, the reinforcement–matrix interface area was larger than in the nanocomposites. Nanotube dispersion had a significant effect on the crystalline structure. In the hybrid composites, the crystallites grew epitaxially on the surface of the well-dispersed carbon nanotubes, which resulted in smaller average crystallite size. On the other hand, the crystallites also grew on the surface of larger carbon nanotube aggregates, which resulted in a larger crystallites in the nanocomposites. In the hybrid composites, smaller crystallites grew on the well-dispersed nanotubes, resulting in an increased rigid amorphous volume fraction. This is a double-layer interphase, where the inner layer is semi-crystalline, and the outer layer is rigid amorphous. Overall, the hybrid composites had better matrix–nanoparticle interaction than the nanocomposites, which was also reflected in their tensile mechanical properties.

Credit author statement

Roland Petrény: Investigation, Writing - Original Draft, Visualization.

László Almásy: Investigation, Writing - Original Draft.

László Mészáros: Conceptualization, Writing - Review & Editing, Supervision.

Declaration of competing interest

The authors declare that they have no known competing financial interests or personal relationships that could have appeared to influence the work reported in this paper.

Acknowledgements

The research reported in this paper is part of project no. BME-NVA-02, implemented with the support provided by the Ministry of Innovation and Technology of Hungary from the National Research, Development and Innovation Fund, financed under the TKP2021 funding scheme. László Mészáros is thankful for János Bolyai Research Scholarship of the Hungarian Academy of Sciences, and for the ÚNKP-21-5 New National Excellence Program of the Ministry for Innovation and Technology. The authors are thankful for Dr. János Madarász (Budapest University of Technology and Economics, Faculty of Chemical Technology and Biotechnology, Department of Inorganic and Analytical Chemistry) for his assistance in performing X-ray diffraction tests.

References

[1] T.F. Qin, H. Wang, J. He, Q.Q. Qu, Y.S. Da, X.Y. Tian, Amino multi-walled carbon nanotubes further improve the thermal conductivity of boron nitride/liquid crystal epoxy resin composites, Express Polym. Lett. 14 (2020) 1169–1179, https://doi.org/10.3144/expresspolymlett.2020.95.

[2] T.T. Koilraj, K. Kalaichelvan, Hybrid nanocomposites – a review, Appl. Mech. Mater. (2015) 766–767. 10.4028/www.scientific.net/AMM.766-767.50, 50–56.

[3] S. Shajari, M. Arjmand, S.P. Pawar, U. Sundararaj, L.J. Sudak, Synergistic effect of hybrid stainless steel fiber and carbon nanotube on mechanical properties and electromagnetic interference shielding of polypropylene nanocomposites, Compos. B Eng. 165 (2019) 662–670, https://doi.org/10.1016/j.compositesb.2019.02.044.

[4] M.R. Zakaria, H. Md Akil, M.H. Abdul Kudus, F. Ullah, F. Javed, N. Nosbi, Hybrid carbon fiber-carbon nanotubes reinforced polymer composites: a review, Compos. B Eng. 176 (2019), 107313, https://doi.org/10.1016/j.compositesb.2019.107313.

[5] J. Szakács, R. Petrény, L. Mészáros, Crystalline properties of melt-processed polyamide 6 matrix multiscale hybrid composites, J. Therm. Anal. Calorim. 137 (2019) 43–53, https://doi.org/10.1007/s10973-018-7911-6.

[6] T. Li, G. Zhao, L. Zhang, G. Wang, B. Li, J. Gong, Ultralow-threshold and efficient EMI shielding PMMA/MWCNTs composite foams with segregated conductive network and gradient cells, Express Polym. Lett. 14 (2020) 685–703, https://doi.org/10.3144/expresspolymlett.2020.56.

[7] A.J. Rodriguez, M.E. Guzman, C.-S. Lim, B. Minaie, Mechanical properties of carbon nanofiber/fiber-reinforced hierarchical polymer composites manufactured with multiscale-reinforcement fabrics, Carbon 49 (2011) 937–948, https://doi.org/10.1016/j.carbon.2010.10.057.

[8] N. Gamze Karsli, S. Yesil, A. Aytac, Effect of hybrid carbon nanotube/short glass fiber reinforcement on the properties of polypropylene composites, Compos. B Eng. 63 (2014) 154–160, https://doi.org/10.1016/j.compositesb.2014.04.006.

[9] N. Rasana, K. Jayanarayanan, K.P. Rajan, A. Gopanna, The rheological behaviour and thermal ageing characteristics of PP/MWCNT/glass fibre multiscale composites, Polym. Polym. Compos. (2021), https://doi.org/10.1177/0967391121992909.

[10] M.J.J. Fernandez, K. Abirami, S. Swetha, S. Soundarya, N. Rasana, K. Jayanarayanan, The effect of nano, micro and dual scale filler reinforcement on the morphology, mechanical and barrier properties of polypropylene composites, Mater. Today Proc. (2019) 5067–5071, https://doi.org/10.1016/j.matpr.2020.10.424.

[11] R. Petrény, L. Mészáros, Moisture dependent tensile and creep behaviour of multi-wall carbon nanotube and carbon fibre reinforced, injection moulded polyamide 6 matrix multi-scale composites, J. Mater. Res. Technol. 16 (2022) 689–699, https://doi.org/10.1016/j.jmrt.2021.12.030.

[12] G.L. Jadav, V.K. Aswal, P.S. Singh, SANS study to probe nanoparticle dispersion in nanocomposite membranes of aromatic polyamide and functionalized silica nanoparticles, J. Colloid Interface Sci. 351 (2010) 304–314, https://doi.org/10.1016/j.jcis.2010.07.028.

[13] A.R. Hopkins, S.J. Tomczak, V. Vij, A.J. Jackson, Small Angle Neutron Scattering (SANS) characterization of electrically conducting polyaniline nanofiber/polyimide nanocomposites, Thin Solid Films 520 (2011) 1617–1620, https://doi.org/10.1016/j.tsf.2011.07.039.

[14] S. Boukheir, A. Len, J. Füzi, V. Kenderesi, M.E. Achour, N. Éber, L.C. Costa, A. Oueriagli, A. Outzourhit, Structural characterization and electrical properties of carbon nanotubes/epoxy polymer composites, J. Appl. Polym. Sci. 134 (2017), 44514, https://doi.org/10.1002/app.44514.

[15] A. Krishnamurthy, R. Tao, E. Senses, S.M. Doshi, F.A. Burni, B. Natarajan, D. Hunston, E.T. Thostenson, A. Faraone, A.L. Forster, A.M. Forster, Multiscale polymer dynamics in hierarchical carbon nanotube grafted glass fiber reinforced composites, ACS Appl. Polym. Mater. 1 (2019) 1905–1917, https://doi.org/10.1021/acsapm.9b00464.

[16] M.K. Hassanzadeh-Aghdam, R. Ansari, M.J. Mahmoodi, Thermo-mechanical properties of shape memory polymer nanocomposites reinforced by carbon nanotubes, Mech. Mater. 129 (2019) 80–98, https://doi.org/10.1016/j.mechmat.2018.11.009.

[17] M.K. Hassanzadeh-Aghdam, M.J. Mahmoodi, R. Ansari, A. Darvizeh, Interphase influences on the mechanical behavior of carbon nanotube–shape memory polymer nanocomposites: a micromechanical approach, J. Intell. Mater. Syst. Struct. 30 (2018) 463–478, https://doi.org/10.1177/1045389X18812704.

[18] M.K. Hassanzadeh-Aghdam, M.J. Mahmoodi, R. Ansari, Creep performance of CNT polymer nanocomposites -An emphasis on viscoelastic interphase and CNT agglomeration, Compos. B Eng. 168 (2019) 274–281, https://doi.org/10.1016/j.compositesb.2018.12.093.

[19] L. Lendvai, Water-assisted production of polypropylene/boehmite composites, Period. Polytech. - Mech. Eng. 64 (2020) 128–135, https://doi.org/10.3311/PPme.13981.

[20] A.-C. Brosse, S. Tencé-Girault, P.M. Piccione, L. Leibler, Effect of multi-walled carbon nanotubes on the lamellae morphology of polyamide-6, Polymer 49 (2008) 4680–4686, https://doi.org/10.1016/j.polymer.2008.08.003.

[21] Melvin I. Kohan. Nylon Plastics Handbook, Hanser/Gardner Publications, Cincinnati, OH, 1995.

[22] D. Kobayashi, A. Takahara, Interphase crystal structure of polyamide 6 on carbon materials revealed by grazing incidence X-ray diffraction with synchrotron radiation, Polymer 97 (2016) 174–178, https://doi.org/10.1016/j.polymer.2016.05.028.

[23] A. O'Neill, D. Bakirtzis, D. Dixon, Polyamide 6/Graphene composites: the effect of in situ polymerisation on the structure and properties of graphene oxide and reduced graphene oxide, Eur. Polym. J. 59 (2014) 353–362, https://doi.org/10.1016/j.eurpolymj.2014.07.038.

[24] H. Chen, P. Cebe, Investigation of the rigid amorphous fraction in Nylon-6, J. Therm. Anal. Calorim. 89 (2007) 417–425, https://doi.org/10.1007/s10973-007-8215-4.

[25] J. Karger-Kocsis, Interphase with lamellar interlocking and amorphous adherent – a model to explain effects of transcrystallinity, Adv. Compos. Lett. 9 (2000), https://doi.org/10.1177/096369350000900307, 096369350000900307.

[26] M.A. Maghsoudlou, R. Barbaz Isfahani, S. Saber-Samandari, M. Sadighi, Effect of interphase, curvature and agglomeration of SWCNTs on mechanical properties of polymer-based nanocomposites: experimental and numerical investigations, Compos. B Eng. 175 (2019), 107119, https://doi.org/10.1016/j.compositesb.2019.107119.

[27] M. Karevan, R. Pucha, M. Bhuiyan, K. Kalaitzidou, Effect of interphase modulus and nanofiller agglomeration on the tensile modulus of graphite nanoplatelets and carbon nanotube reinforced polypropylene nanocomposites, Carbon Lett. 11 (2010) 325–331, https://doi.org/10.5714/CL.2010.11.4.325.

[28] J. Szakács, L. Mészáros, Synergistic effects of carbon nanotubes on the mechanical properties of basalt and carbon fiber-reinforced polyamide 6 hybrid composites, J. Thermoplast. Compos. Mater. 31 (2017) 553–571, https://doi.org/10.1177/0892705717713055.

[29] L. Rosta, Cold neutron research facility at the Budapest Neutron Centre, Appl. Phys. A 74 (2002) s52–s54, https://doi.org/10.1007/s003390201387.

[30] L. Almásy, New Measurement Control Software on the Yellow Submarine SANS Instrument at the Budapest Neutron Centre, J. Surf. Investig. 15 (2021) 517–531, https://doi.org/10.1134/S1027451021030046.

[31] S. Park, J.O. Baker, M.E. Himmel, P.A. Parilla, D.K. Johnson, Cellulose crystallinity index: measurement techniques and their impact on interpreting cellulase performance, Biotechnol. Biofuels 3 (2010) 10, https://doi.org/10.1186/1754-6834-3-10.

[32] P.M.A. Sherwood, Rapid evaluation of the Voigt function and its use for interpreting X-ray photoelectron spectroscopic data, Surf. Interface Anal. 51 (2019) 254–274, https://doi.org/10.1002/sia.6577.

[33] H. Kursun, U. Ulusoy, Influence of shape characteristics of talc mineral on the column flotation behavior, Int. J. Miner. Process. 78 (2006) 262–268, https://doi.org/10.1016/j.minpro.2005.11.003.

[34] F.T.L. Muniz, M.A.R. Miranda, C. Morilla dos Santos, J.M. Sasaki, The Scherrer equation and the dynamical theory of X-ray diffraction, Acta Crystallogr. A 72 (2016) 385–390, https://doi.org/10.1107/S205327331600365X.

[35] T. Fornes, D. Paul, Crystallization behavior of nylon 6 nanocomposites, Polymer 44 (2003) 3945–3961, https://doi.org/10.1016/S0032-3861(03)00344-6.

[36] L. Mandelkern, Kinetics and Mechanisms. Crystallization of Polymers second ed., vol. 2, Cambridge University Press, Cambridge, 2004.

[37] T. Itoh, H. Miyaji, K. Asai, Thermal properties of α- and γ-forms of nylon 6, Jpn. J. Appl. Phys. 14 (1975) 206–215, https://doi.org/10.1143/jjap.14.206.

[38] G. Von White, F.S. Mohammed, C.L. Kitchens, Small-angle neutron scattering investigation of gold nanoparticle clustering and ligand structure under antisolvent conditions, J. Phys. Chem. C 115 (2011) 18397–18405, https://doi.org/10.1021/jp112020r.

[39] F. Gabel, Chapter thirteen - Small-angle neutron scattering for structural biology of protein–RNA complexes, in: S.A. Woodson, F.H.T. Allain (Eds.), Structures of Large RNA Molecules and Their Complexes, Academic Press, 2015, pp. 391–415.

[40] Y. Li, W.A. Goddard, Nylon 6 crystal structures, folds, and lamellae from theory, Macromolecules 35 (2002) 8440–8455, https://doi.org/10.1021/ma020815n.